# Propagation of Local Bubble Parameters of Subcooled Boiling Flow in a Pressurized Vertical Annulus Channel

In-Cheol Chu*, Seung Jun Lee, Young Jung Youn, Jong Kuk Park, Hae Seob Choi and Dong Jin Euh
*Korea Atomic Energy Research Institute, Thermal Hydraulics Safety Research Division,*
*989-111 Daedeok-daero, Yuseong-gu, Daejeon, 305-353, Korea*
**Corresponding author: chuic@kaeri.re.kr*

## 1. Introduction

Owing to the high efficiency of heat transfer, subcooled boiling flow appears in many industrial and engineering systems, including nuclear power plants. Local bubble parameters such as void fraction, bubble velocity, interfacial area concentration, and Sauter mean diameter are important to determine the heat and momentum transfer performance of the systems.

Recently, CMFD (Computation Multi-Fluid Dynamics) tools have been being developed to simulate two-phase flow safety problems in nuclear reactor, including the precise prediction of local bubble parameters in subcooled boiling flow [1-6].

However, a lot of complicated phenomena are encountered in the subcooled boiling flow such as bubble nucleation and departure, interfacial drag of bubbles, lateral migration of bubbles, bubble coalescence and break-up, and condensation of bubbles, and the constitutive models for these phenomena are not yet complete. As a result, it is a difficult task to predict the radial profile of bubble parameters and its propagation along the flow direction.

Several experiments were performed to measure the local bubble parameters for the validation of the CMFD code analysis and improvement of the constitutive models of the subcooled boiling flow, and to enhance the fundamental understanding on the subcooled boiling flow [7-12]. However, the experimental data on the propagation of the local flow parameters at elevated pressure condition is still lacking.

DEBORA experiments [7] were performed in a heated vertical tube using R-12 as working fluid. Radial profile of local flow parameters were measured at the end of the heated section. They suggested similarity criteria for pressure scaling by the phasic density ratio and heat flux scaling by boiling number (*Bo*). The pressure of the experiments was in the range of 1.4 to 3.0 MPa, which is equivalent to the pressure of 10 to 18 MPa of subcooled boiling flow in PWRs. In addition, according to their heat flux scaling criterion, the high heat flux subcooled boiling flow in PWRs can be simulated at about ten times smaller heat flux condition in DEBORA experiments. The information on the propagation of the local flow parameters along the flow direction was not provided because the measurements were conducted at the fixed elevation.

In SUBO experiments [11, 12], the radial profiles of local bubble parameters, liquid velocity and temperature were obtained for steam-water subcooled boiling flow in a vertical annulus. The local flow parameters were measured at six elevations along the flow direction. The pressure was in the range of 0.15 to 0.2 MPa.

We have launched an experimental program to investigate quantify the local subcooled boiling flow structure under elevated pressure condition in order to provide high precision experimental data for thorough validation of up-to-date CMFD codes. In the present study, the first set of experimental data on the propagation of the radial profile of the bubble parameters was obtained for the subcooled boiling flow of R-134a in a pressurized vertical annulus channel.

## 2. Experiments

The present boiling test facility consists mainly of a boiling flow loop, a test section, a direct current (DC) power supply, measurement instruments, a control and data acquisition system. The design pressure of the facility is 4.5 MPa and Freon R-134a is used as working fluid.

The boiling flow loop consists of two non-seal canned motor pumps, an accumulator, two pre-heaters, a coriolis mass flow meter of Rheonik Inc., a condenser, two coolers, by-pass pipe lines, and three flow control valves and three manual valves (Fig. 1).

The geometry of the test section is a vertical annulus channel. A Joule heating tube is located at the center of an outer pipe, thus forming an annulus channel. The inner diameter of the outer pipe is 27.2 mm, and the outer diameter of the heating tube is 9.5 mm. The total distance between the inlet and outlet of the test section is 2,880 mm. The test section has four measurement stations at which local bubble parameters are measured and global boiling structure are visualized. The distance between each measurement station is 500 mm. The distance from the test section inlet to the center of the first measurement station is 1,090 mm.

As shown in Figs. 2 and 4, each measurement station is equipped with an optical fiber probe to measure the radial profiles of the bubble parameters such as void fraction, bubble passing frequency, bubble velocity, interfacial area concentration, Sauter mean diameter. Single sensor optical fiber probes are installed at the first and second measurement stations, and double sensor optical fiber probes are installed at the third and fourth measurement stations. Each probe can be moved back and forth in radial direction with a resolution of

0.002 mm using a PLC based servo motor traverse system. The actual traversed distance of the probe is confirmed by a digital dial gauge attached to the probe and the traversing axis, and the resolution of the gauge is 0.001 mm. The typical shape of the double sensor optical fiber probe is shown in Fig. 2. The vertical and horizontal distances between the probe tips are about 400 μm and 150 μm, respectively. Double pressure boundary windows are adopted at two opposite sides of each measurement station for the visualization of the global boiling structure. The inner curvature of the inside visualization window is 27.2 mm which is the same with the inner diameter of the outer pipe. A set of a high speed video camera and a Xenon HID lamp is installed at each measurement station. However, the high speed visualization has not yet conducted in this phase of experiments.

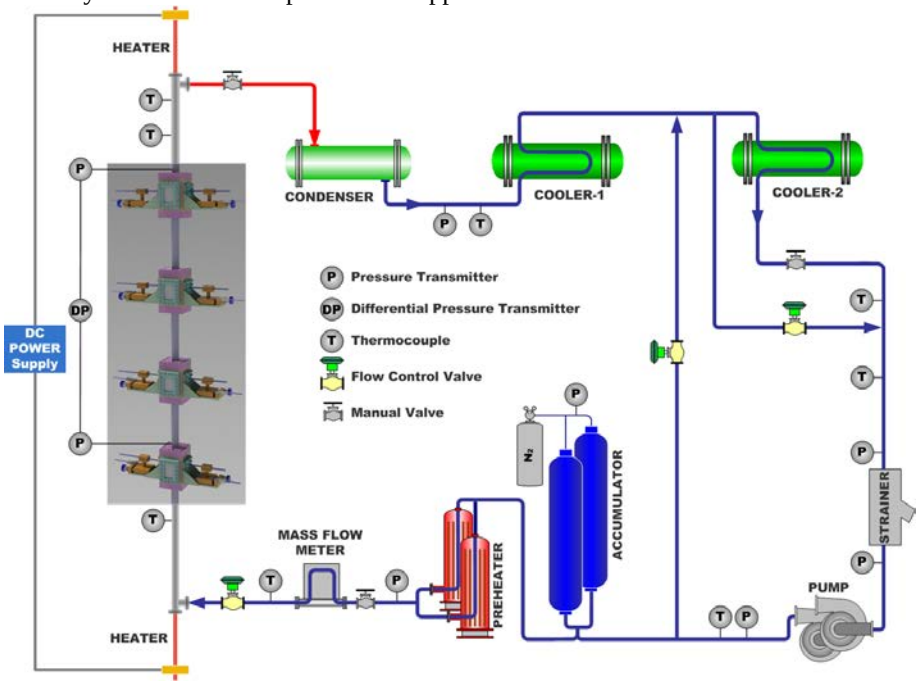


Fig. 1. Schematic of the Test Facility.

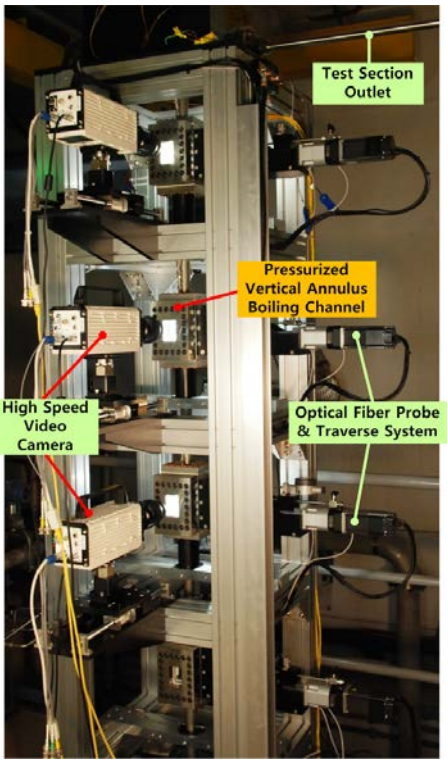


Fig. 2. Photo of the Test Section.

Fig. 3. Photo of the Optical Fiber Probe.

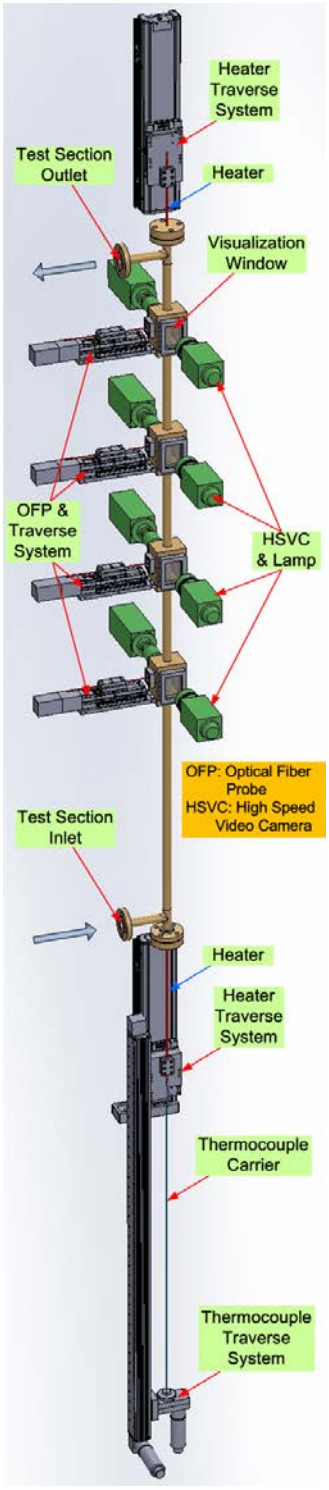


Fig. 4. Schematic of the Test Section.

The total length of the heating tube is 3,900 mm, and the actual heating length is 1,750 mm. The heating tube has non-heating regions of 1,350 mm at the test section inlet side and 800 mm at the test section outlet side. Four spacers (one spacer for each measurement station) were installed to locate the heating tube at the channel center and to prevent the vibration of the heating tube which could be induced by the boiling flow. Each spacer is placed 50 mm above the tip of the optical fiber probe. The spacer was designed to minimize the disturbance to the flow field.

The heating tube can move up and down through the test section without leakage of the working fluid even at high pressure condition. For this movement of the heating tube, two PLC based servo motor traverse systems for the heating tube are installed at the top and bottom of the test section, respectively (Fig. 4). The resolution of the heating tube traverse is less than 0.01 mm. The total span of the heating tube movement is 550 mm, which covers the distance between each measurement station. Therefore, by moving the heating tube up and down, the radial profile of the bubble parameters can be measured at any location of the heating region of the heating tube with the four sets of optical fiber probes spaced with 500 mm interval.

Three fixed thermocouples are installed at the location of 30 mm below the top end of the heating region of the heating tube to detect the critical heat flux occurrence and protect the heating tube from burnout. Two moving thermocouples are installed inside the heating tube. These thermocouples are tightly contacted to the inner surface of the heating tube to measure the local wall temperature distribution of the heating tube. These thermocouples can move up and down from the location of 45 mm above the bottom end of the heating region of the heating tube to the location of 40 mm below the top end of the heating region. In addition, these thermocouples can be rotated 360 degree at any elevation. Thermocouple traverse system is installed below the test section for this thermocouple movement and rotation (Fig. 4). However, the measurement of the local wall temperature distribution was not conducted in this phase of the experiments.

The inlet and outlet temperatures at the test section are measured by type-T thermocouples of Watlow, Inc., the inlet and outlet pressures at the test section are measured by pressure transmitters of Rosemount, Inc., and the pressure difference between the inlet and outlet is measured by differential pressure transmitter of Rosemount, Inc. (Fig. 1). The locations of temperature and pressure measurement in the boiling flow loop are also illustrated in Fig. 1.

The flow rate to the test section is controlled by adjusting the rotation speed of the pump impeller and the opening of the flow control valves. The system pressure is controlled by the accumulator. The fluid temperature to the test section is controlled by adjusting the pre-heater power and the cooling water flow rate to the shell-tube type condenser and coolers. The heat flux of the heater rod is controlled by adjusting the DC voltage of the power supply. The capacity of the power supply is 60 volt and 1,000 ampere.

The present control system consists of several PLC based PID controllers, and the data acquisition system consists of HP 3852a Data Acquisition/Control Unit and a personal computer (PC). The communication and data transfer between the HP 3852a and PC are conducted by HP VEE graphic program via GPIB interface. The optical fiber probes fabricated in KAERI (Korea Atomic Energy Research Institute) are used. The optoelectronic amplifiers, data acquisition board, and data processing software of RBI Instrumentation are used.

Three tests were conducted, and the test condition is presented in Table 1. The values in the parentheses are the ratio of the standard deviation to the mean value of each parameter. According to the similarity criteria suggested in DEBORA experiments [7], the present test conditions are equivalent to the conditions presented in Table 2 for the subcooled boiling flow of water. The pressure of 'Test-03' is similar to the normal operating pressure condition of PWRs.

Table 1: Test Conditions

| | Exit Pressure [MPa] | Mass Flux [kg/m$^2$s] | Heat Flux [kW/m$^2$] | Inlet / Outlet Subcooling [$^o$C] |
|---|---|---|---|---|
| Test-01 | 1.29 (0.11%) | 998 (0.29%) | 120.4 (0.46%) | 12.4 / 4.8 |
| Test-02 | 1.49 (0.13%) | 149 (0.95%) | 60.6 (0.95%) | 27.4 / 3.1 |
| Test-03 | 2.69 (0.12%) | 999 (0.20%) | 120.7 (0.59%) | 8.0 / 2.7 |

Table 2: Test Conditions Equivalent to Water

| | Exit Pressure [MPa] | Mass Flux [kg/m$^2$s] | Heat Flux [kW/m$^2$] |
|---|---|---|---|
| Test-01 | 7.95 | 1425 | 1620 |
| Test-02 | 9.10 | 213 | 815 |
| Test-03 | 15.60 | 1395 | 1550 |

In the present experiments, the location of the heating tube was adjusted to the elevation where the optical fiber probes in the first and fourth measurement stations were located to the position of 230 mm and 1,730 mm above the bottom end of the heating region, respectively. Each optical probe was finely traversed in radial direction so that they are 0.7 mm apart from the outer surface of the heating tube. When the test parameters in Table 1 reached a steady state condition, the radial profiles of bubble parameters were measured by traversing the optical fiber probes in radial direction toward the outer pipe. The measurement was performed at fourteen radial positions and the data was taken for 60 seconds at each radial position. Then, the electric

heating tube was traversed upward by 250 mm, and the measurement of the radial profiles of bubble parameters was repeated. As a result, the radial profiles of bubble parameters were obtained at 7 elevations with 250 mm interval.

## 3. Results and Discussion

Time averaged void fraction, bubble passing frequency, bubble velocity, interfacial area concentration, and Sauter mean diameter at local radial position were evaluated from the time domain void signals of the optical fiber probes under the assumptions that the bubbles are spherical, every part of the bubble has equal probability of penetrating the probe tip, and the bubbles move in the same direction at which the probes are aligned.

The radial profiles of non-dimensional void fraction ($\alpha^*$) and the propagation along the flow direction for each test are presented in Fig. 5. The void fraction ($\alpha$) was non-dimensionalized by the reference void fraction ($\alpha_{ref}$) which corresponded to the void fraction measured in Test-01 at the radial position of 0.7 mm and the elevation of 1730 mm. The origin of the non-dimensional radial position (*i.e.*, $r^* = 0$) corresponds to the outer surface of the heating tube, and the position where $r^*$ is 1 corresponds to the inner surface of the outer pipe.

The general trend of the radial profiles of void fraction was similar for the different measurement elevation of each test. That is, for a given measurement elevation, the void fraction has a maximum value at the measurement position closest to the outer surface of the heating tube (i.e., $r$ = 0.7 mm) and it decreases as the measurement position moves outward. It is due to the fact that the bubbles generated on the surface of the heating tube migrate toward the outer pipe by the non-drag forces such as turbulent dispersion force, shear lift force and virtual mass force, and more bubbles disappear as they migrate further due to the condensation in the subcooled liquid flow.

Further investigation is necessary to check whether the void fraction becomes lower owing to the wall lift force (or wall lubrication force) if the measurement position is moved closer to the outer surface of heating tube. In addition, if we look at the void fraction at the radial position of $r$ = 0.7 mm, the void fraction is not always ordered in accordance with the order of the elevation. Further study is also necessary to find out the cause of this phenomenon.

As expected, the area averaged void fraction became higher and the bubble layer became thicker as the distance from the bottom end of the heating tube increased because the subcooling of the liquid flow became lower with the increase of the elevation, and the accumulated net vapor generation amount increased with the increase of the elevation.

Comparing the void fraction profiles obtained from Test-01 and Test-03, the pressure effect on the radial profile and the propagation of void fraction does not seem to be significant when the mass flux, heat flux, and liquid subcooling are similar. However, compared with the results of Test-01, the void fraction itself, and its radial profile and axial propagation of Test-02 were remarkably changed due to the significant changes in the mass flux, heat flux, and liquid subcooling.

The reduction ratio of the void fraction close to the heating surface at the elevation of 1,730 mm was similar to the reduction ratio of heat flux though the mass flux was reduced to one seventh. However, the reduction of the void fraction was much higher than the reduction ratio of the heat flux at lower elevation because the liquid subcooling was higher in Test-02 than Test-01. Therefore, we can deduce that the heat flux and liquid subcooling have greater influence on the void fraction near the heating surface than the liquid velocity.

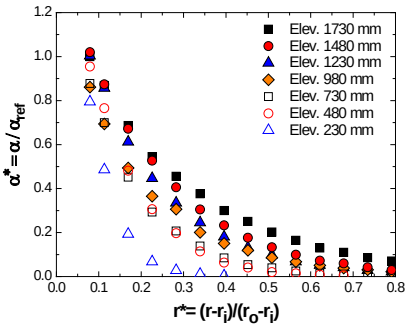


(a) Test-01

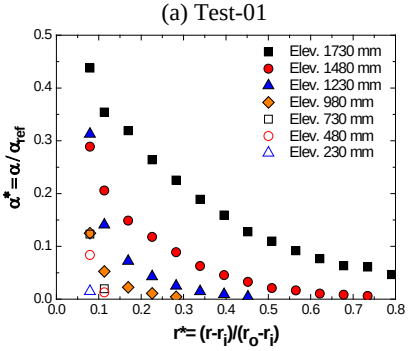


(b) Test-02

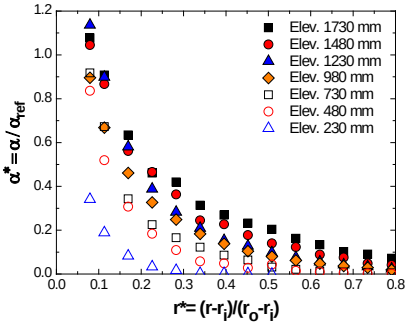


(c) Test-03

Fig. 5. Radial Profiles of Void Fraction.

As shown in Fig. 6, the radial profile and the axial propagation of bubble passing frequency are qualitatively similar to those characteristics of void fraction. However, the quantitative characteristics are quite different, and it is because that the bubble passing

frequency is determined by the void fraction, bubble velocity, and bubble size. That is, the bubble passing frequency is proportional to the void fraction and bubble velocity, and inversely proportional to the bubble size. Thus, the bubble passing frequency at the elevation of 1,730 mm of Test-02 was decreased by about one seventh mainly by the influence of void fraction and bubble velocity. The bubble passing frequency at the elevation of 1,730 mm of Test-03 showed about a twofold increase mainly by the change of bubble size, as will be discussed later.

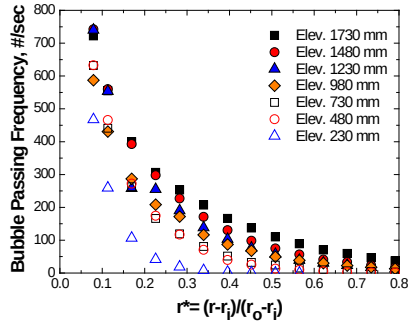


(a) Test-01

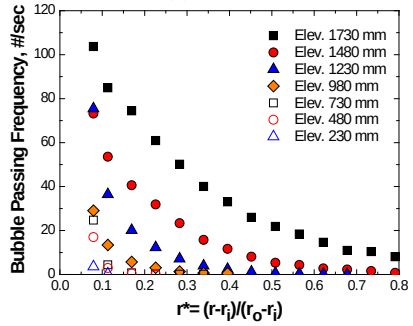


(b) Test-02

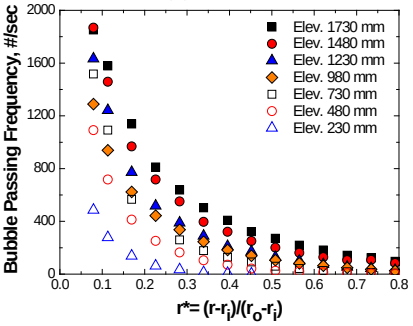


(c) Test-03

Fig. 6. Radial Profiles Bubble Passing Frequency.

The radial profiles of bubble velocity are shown in Fig. 7 for each test. The time averaged bubble velocity at local radial position ($V_B = D_{tip} / T_{flight}$) was calculated by the distance between the front and the rear sensors ($D_{tip}$) and the time of flight ($T_{flight}$). The time of flight is an average transit time for the bubbles to move from the front sensor to the rear sensor, and it is determined by the cross-correlation of the time domain void signals of two sensors.

In case of Test-01 and Test-03, the absolute value and the shape of the radial profile were similar to each other. The local bubble velocity is determined by the local liquid velocity, buoyancy, and interfacial drag. The interfacial drag coefficient in bubbly flow is governed by void fraction and bubble Reynolds number. We can expect that the liquid velocity would not be much different for both the cases of Test-01 and Test-03 because the mass flux is almost same and the difference in the liquid density is about 20%. However, the bubble size of Test-03 was about the half of the bubble size of Test-01 as shown in Fig. 9, which definitely affected the buoyancy and interfacial drag. Then, it could be explained by the fact that the differences in thermodynamic properties such as kinematic viscosity and phasic density difference between two test conditions compensated the differences caused by the bubble size change.

There was a significant difference in the bubble velocities of Test-01 and Test-02 because, as expected, the liquid velocity and void fraction were quite different. Another interesting thing is that the peak bubble velocity appeared at the non-dimensional radial position ($r^*$) between 0.3 and 0.35 in Test-01 whereas the peak shifted to the position ($r^*$) between 0.15 and 2.0.

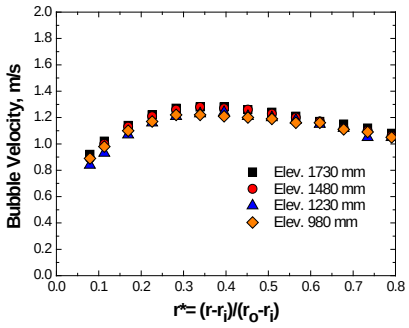


(a) Test-01

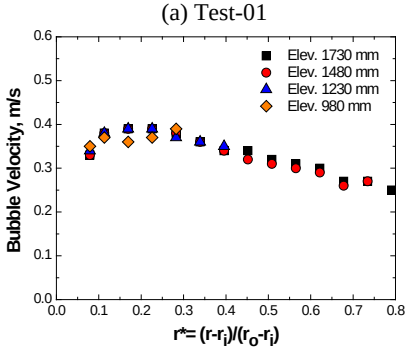


(b) Test-02

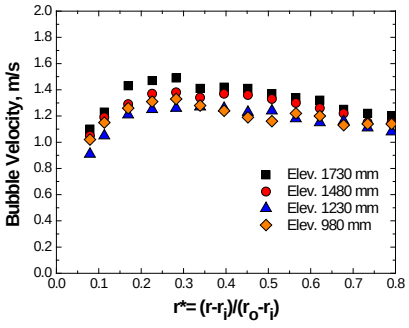


(c) Test-03

Fig. 7. Radial Profiles of Bubble Velocity

The radial profiles of non-dimensional interfacial area concentration ($a_i$*) and its axial propagation for each test are presented in Fig. 8. The interfacial area concentration ($a_i$) was non-dimensionalized by the reference interfacial area concentration ($a_{i,ref}$) which corresponded to the interfacial area concentration measured in Test-01 at the radial position of 0.7 mm and the elevation of 1730 mm. The time averaged interfacial area concentration at local radial position ($a_i = 4f_B / V_B$) was calculated by the bubble passing frequency ($f_B$) and the bubble velocity ($V_B$). The interfacial area concentration is proportional to the void fraction and inverse of bubble size because the bubble passing frequency is proportional to the void fraction, bubble velocity, and inverse of bubble size.

Compared with the axial propagation (or evolution) of the interfacial area concentration in Test-01 and Test-03, the propagation in Test-02 was much significant. It is mainly due to the fact that the liquid subcooling in Test-02 experienced more dramatic change in the flow direction, which directly affected the axial propagation of the void fraction.

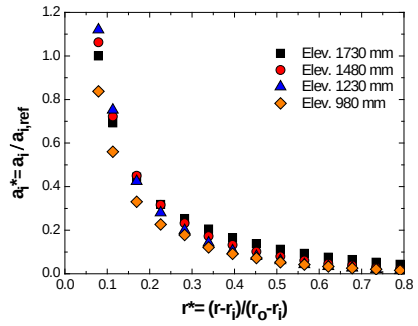


(a) Test-01

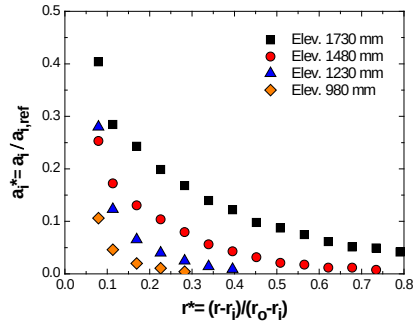


(b) Test-02

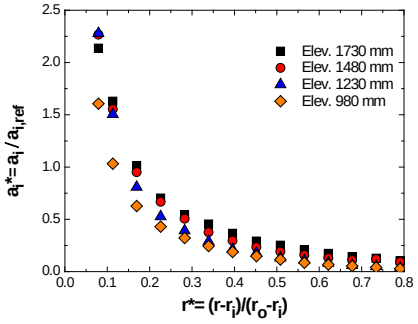


(c) Test-03

Fig. 8. Radial Profiles of Interfacial Area Concentration.

The heat flux of Test-02 was about the half of Test-01. The liquid subcooling of Test-02 was lower than Test-01 except the subcooling at the elevation of 1,730 mm, and the difference of subcooling became larger at lower elevation. The effects of the heat flux and liquid subcooling are reflected in the results of the radial profiles of the void fraction and interfacial area concentration and their axial propagation, as shown in Figs. 5 and 8. The interfacial area concentration of Test-03 showed about twofold increase compared with that of Test-01, and it was mainly due to the fact that the bubble size was reduced by the half with an increase of the system pressure.

The radial profiles of non-dimensional Sauter mean diameter ($D_{sm}$*) and its axial propagation for each test are presented in Fig. 9. The Sauter mean diameter ($D_{sm}$) was non-dimensionalized by the reference interfacial area concentration ($D_{sm,ref}$) which corresponded to the Sauter mean diameter measured in Test-01 at the radial position of 0.7 mm and the elevation of 1730 mm. The time averaged Sauter mean diameter at local radial position ($D_{sm} = 6\alpha / a_i$) was calculated by the void fraction ($\alpha$) and the interfacial area concentration ($a_i$).

The bubble size near the heating surface is mainly governed by the bubble size at the departure (or lift-off), and the bubble size changes by the bubble coalescence and break-up, and by the condensation as the bubbles migrate toward the outer pipe. In case of Test-01, the Sauter mean diameter increased as the bubbles moved from the heating surface to the central region of the channel, and the diameter showed the peak at the radial position ($r$*) of around 0.3 to 0.4. Then, the diameter decreased with the further increase of the radial position. Based on this observation, we can deduce the followings: (1) In the region where $r$* is smaller than 0.3, the bubbles had sufficient population and collision frequency so that the coalescence effect was dominant over the effects of break-up and condensation, thus the bubble size increased in this region; (2) In the other region where $r$* is larger than 0.4, the coalescence effect became minor due to the decrease in the bubble population and collision frequency, thus the bubble size decreased in this region.

For the elevations of 980 mm, 1,230 mm, and 1,480 mm of Test-02, the radial profiles of bubble size showed a maximum value at the position closest to the heating surface, and then it decreased monotonically with an increase of the radial position. This would be due to the fact that the condensation effect became dominant by the increase of liquid subcooling, and the coalescence effect was minor because the bubble population and collision frequency were low even at the position close to the heating surface.

The trend of the radial profile of bubble size in Test-03 was similar to that in Test-01. However, the absolute bubble size was about the half of the bubble size in Test-01. This implies that the pressure effect on the bubble size was significant because the mass flux, heat flux, and liquid subcooling in Test-03 were similar to

those in Test-01. According to the observation of Ahmadi et al. [13] for single isolated bubble regime of subcooled boiling flow, the size of bubble was significantly dependent on the pressure and the size became one order of magnitude smaller when the pressure increased from atmospheric condition to the elevated pressure condition of 0.8 MPa. It would be reasonable to think that the reduction of the bubble size in Test-03 was caused mainly by the increase of pressure.

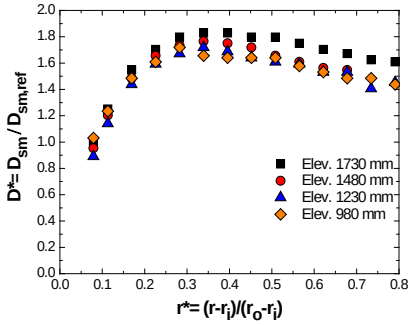


(a) Test-01

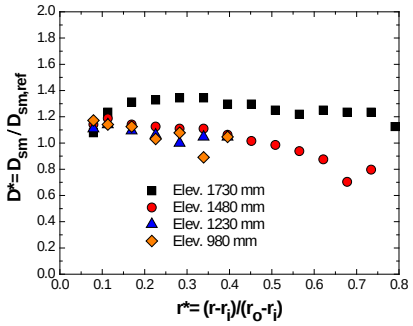


(b) Test-02

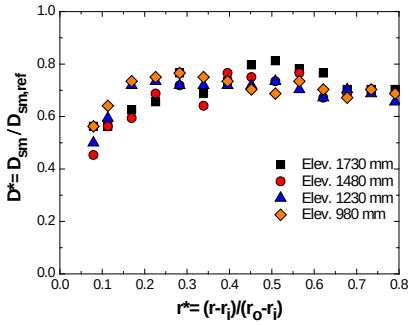


(c) Test-03

Fig. 9. Radial Profiles of Sauter Mean Diameter.

## 4. Conclusions

An experimental program was launched for an in-depth investigation of a subcooled boiling flow in an elevated pressure condition. Unique experimental data on the radial profiles of bubble parameters and their axial propagation were obtained for a wide range of pressure, heat flux, mass flux, and liquid subcooling. According to the similarity criteria, the pressure condition of the present experiments which used R-134a covered the normal operating pressure of PWRs.

Depending on the test condition, significant variations were observed on the distribution and propagation of the bubble parameters such as void fraction, bubble passing frequency, bubble velocity, interfacial area concentration, and Sauter mean diameter. Effect of pressure on Sauter mean diameter and interfacial area concentration was manifested.

Further effort will be pursued to obtain more detailed data such as visualization of global boiling phenomena and detailed wall temperature distribution for wider range of experimental condition. The local boiling structure of DNB (departure from nucleate boiling) at PWR operating pressure condition will be one of the targets of future research.

We expect that the present experimental data and the data obtained in the future will be useful for the thorough validation and improvement of CMFD codes and constitutive relations.

## REFERENCES

[1] C. Morel, W. Yao, and D. Bestion , Three Dimensional Modeling of Boiling Flow for the NEPTUNE Code, Proceedings of the 10th International Topical Meeting on Nuclear Reactor Thermal Hydraulics, October 5-11, 2003, Seoul, Korea.

[2] B.-U. Bae, B.-J. Yun, H.-Y. Yoon, C.-H. Song, and G. C. Park, Analysis of Subcooled Boiling Flow with One-Group Interfacial Area Transport Equation and Bubble Lift-off Model, Nuclear Engineering and Design, Vol. 240, p. 2281, 2010.

[3] D. Prabhudharwadkar, M. A. Lopez, J. Buchanan Jr., and A. Vaidheeswaran, Assessment of Components of the Subcooled Boiling Model for CFD Simulations, Proceedings of the 14th International Heat Transfer Conference, August 8-13, 2010, Washington D.C., USA.

[4] E. Krepper and R. Rzehak, CFD for Subcooled Flow Boiling: Simulation of DEBORA Experiments, Nuclear Engineering and Design, Vol. 241, p. 3851, 2011.

[5] B.-J. Yun, A. Splawski, S. Lo, and C.-H. Song, Prediction of a Subcooled Boiling Flow with Advanced Two-Phase Flow Models, Nuclear Engineering and Design, Vol. 252, p. 351, 2012.

[6] E. Krepper, R. Rzehaka, C. Lifante, and T. Frank, CFD for Subcooled Flow Boiling: Coupling Wall Boiling and Population Balance Models, Nuclear Engineering and Design, Vol. 255, p. 330, 2013.

[7] J. Garnier, E. Manon, and G. Cubizolles, Local Mesaurements on Flow Boiling of Refrigerant 12 in a Vertical Tube, Multiphase Science and Technology, Vol. 13, p. 1, 2001.

[8] T. H. Lee, G. C. Park, and D. J. Lee, Local Flow Characteristics of Subcooled Boiling Flow of Water in a Vertical Concentric Annulus, International Journal of Multiphase Flow, Vol. 28, p. 1351, 2002.

[9] R. P. Roy, S. Kang, J. A. Zarate, and A. Laporta, Turbulent Subcooled Boiling Flow–Experiments and Simulation, Journal of Heat Transfer, Vol. 124, p. 73, 2002.

[10] R. Situ, T. Hibiki, X. Sun, Y. Mi, and M. Ishii, Flow Structure of Subcooled Boiling Flow in An Internally Heated Annulus, International Journal of Heat and Mass Transfer, Vol. 47, p. 5351, 2004.

[11] B.-J. Yun, B.-U. Bae, D.-J. Euh, G. C. Park, and C.-H. Song, Characteristics of the Local Bubble Parameters of a

Subcooled Boiling Flow in an Annulus, Nuclear Engineering and Design, Vol. 240, p. 2295, 2010.
[12] B.-J. Yun, B.-U. Bae, D.-J. Euh, and C.-H. Song, Experimental Investigation of Local Two-Phase Flow Parameters of a Subcooled Boiling Flow in an Annulus, Nuclear Engineering and Design, Vol. 240, p. 3956, 2010.
[13] R. Ahmadi, T. Ueno, and T. Okawa, Bubble Dynamics at Boiling Incipience in Subcooled Upward Flow Boiling, International Journal of Heat and Mass Transfer, Vol. 55, p. 488, 2012.